

Dynamic crushing of sandwich panels with prismatic lattice cores

M.T. Tilbrook *, D.D. Radford, V.S. Deshpande, N.A. Fleck

Department of Engineering, University of Cambridge, Trumpington Street, Cambridge CB2 1PZ, UK

Received 16 November 2006; received in revised form 24 January 2007

Available online 13 February 2007

Abstract

The dynamic out-of-plane compressive response of stainless steel corrugated and Y-frame sandwich cores have been investigated for impact velocities ranging from quasi-static to 200 ms^{-1} . Laboratory-scale sandwich cores of relative density 2.5% were manufactured and the stresses on the front and rear faces of the dynamically compressed sandwich cores were measured using a direct impact Kolsky bar. Direct observational evidence is provided for micro-inertial stabilisation of both topologies against elastic buckling at impact velocities below 30 ms^{-1} . At higher impact velocities, plastic waves within the core members result in the front face stresses increasing with increasing velocity while the rear face stresses remain approximately constant. While the finite element calculations predict the rear face stresses and dynamic deformation modes to reasonable accuracy, the relatively slow response time of the measurement apparatus results in poor agreement between the measured and predicted front face stresses. The finite element calculations also demonstrate that material strain-rate effects have a negligible effect upon the dynamic compressive response of laboratory-scale and full-scale sandwich cores.

© 2007 Published by Elsevier Ltd.

Keywords: Lattice cores; Impact testing; Dynamic loads; Material rate-dependence; Dynamic buckling

1. Introduction

Clamped plates are representative of the structures used in the design of commercial and military vehicles. For example, the outermost structure on a ship comprises plates welded to an array of stiffeners. Recent investigations have revealed that metallic sandwich panels have structural advantages over monolithic plates of equal mass in blast resistant structural applications (Xue and Hutchinson, 2004; Deshpande and Fleck, 2005). Prismatic core topologies are considered ideal for application in blast resistant sandwich beams as they provide high longitudinal shear and stretching strengths. Moreover, these cores can be manufactured at length scales that would be typical in most marine applications. The present study is a combined numerical and

* Corresponding author. Tel.: +44 1223 339883; fax: +44 1223 332662.

E-mail addresses: mtt25@cam.ac.uk, mttilbrook@gmail.com (M.T. Tilbrook).

experimental investigation into the dynamic compressive response of two prismatic sandwich cores: the corrugated and Y-frame sandwich cores.

The dynamic out-of-plane compressive response of a variety of stainless steel lattice cores has been explored over the last few years. For example, Radford et al. (2006), Ferri et al. (2007) and Lee et al. (2006) have investigated the dynamic response of square-honeycomb core, the I-core and the pyramidal truss core via direct impact Kolsky bar experiments and finite element calculations. These studies have demonstrated that micro-inertial stabilisation significantly delays the onset of buckling in these lattice cores; consequently, the dynamic strength exceeds the quasi-static strength by nearly a factor of four at impact velocities around 50 ms^{-1} . While Ferri et al. (2007) limited their attention to the forces on the distal end of the impact, Radford et al. (2006) and Lee et al. (2006) measured the forces on both the impacted and distal faces of the sandwich cores. The experiments of Radford et al. (2006) demonstrated that the peak stress on the impacted (front) face increases approximately linearly with impact velocity while the distal (rear) face stress remains approximately constant: plastic wave effects play a significant role at these impact velocities. The investigations of Radford et al. (2006) and Ferri et al. (2007) also highlighted the interactions of micro-inertial stabilisation against buckling and plastic wave effects. This interaction gives rise to the so-called “buckle waves” as analysed by Vaughn and Hutchinson (2006).

Optimisation studies by Fleck and Deshpande (2004) and Xue and Hutchinson (2004) have revealed that sandwich panels with prismatic corrugated cores (also known as folded-plate cores) are promising for blast resistant sandwich plates due to their high compressive, longitudinal shear and axial strengths. Recent experimental investigations by Rubino et al. (2006) have shown that clamped sandwich beams comprising the Schelde¹ Y-frame core have nearly identical dynamic resistances (in terms of the deflections of the beams when impacted by metal foam projectiles) to corrugated core sandwich beams of equal mass. Both types of beams significantly outperform monolithic beams of equal mass: for a given blast impulse, the corrugated and Y-frame sandwich beams undergo significantly smaller deflections. However, no experimental or computational investigations into the dynamic responses of these lattice cores have been reported to date; this is the focus of the present study.

The outline of the paper is as follows. First, the dynamic out-of-plane compressive response of corrugated and Y-frame lattice cores of relative density $\bar{\rho} = 0.025$ is investigated for applied compressive velocities ranging from quasi-static to 200 ms^{-1} . The stresses transmitted by the impacted and distal ends of the specimens are measured using a direct impact Kolsky bar, and high speed photography is employed to observe the dynamic deformation modes. The experimental measurements are compared with finite element simulations to gauge the fidelity of the simulations and to help interpret the experimental findings. Subsequently, the finite element calculations are used to predict scale effects in the dynamic compression of these lattice cores and to relate laboratory-scale results to the response of full-scale marine structures.

2. Experimental methods and measurements

2.1. Specimen manufacture

The geometries of the corrugated and Y-frame specimens are sketched in Figs. 1a and b, respectively. Both sandwich cores have an effective relative density (ratio of density of the “smear-out” core to that of the solid material from which it is made) of $\bar{\rho} = 2.5\%$ and overall dimensions: (a) height $H = 22 \text{ mm}$; (b) width $W = 52 \text{ mm}$ (Y-frame core) and $W = 50.8$ (corrugated core); and (c) depth (normal to the plane of the paper) $b = 54 \text{ mm}$. The specimens were manufactured from 304 stainless steel sheets of thickness $t = 0.30 \text{ mm}$ using the fabrication techniques of Rubino et al. (2006).

The corrugated core specimens were manufactured in two steps. First, stainless steel sheets of thickness 0.3 mm were CNC folded to produce a corrugated sheet with a corrugation angle $\omega = 60^\circ$. A sandwich specimen was constructed by brazing this corrugated sheet to 0.3 mm thick 304 stainless face-sheets. The Ni–Cr25–

¹ Royal Schelde, P.O. Box 16 4380 AA Vlissingen, The Netherlands.

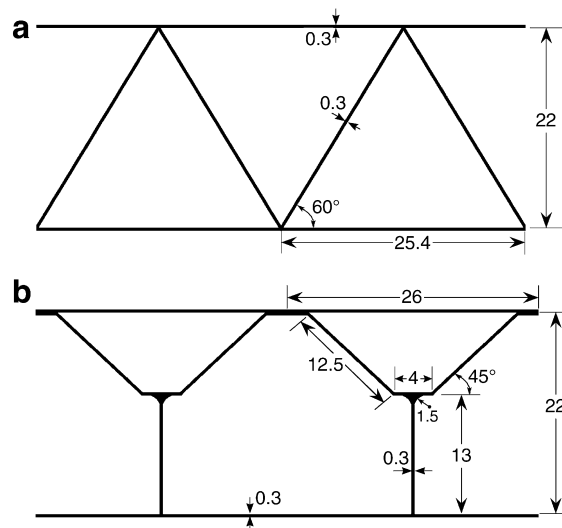


Fig. 1. Geometries of the (a) corrugated and (b) Y-frame sandwich cores investigated in this study. All dimensions are in millimeters.

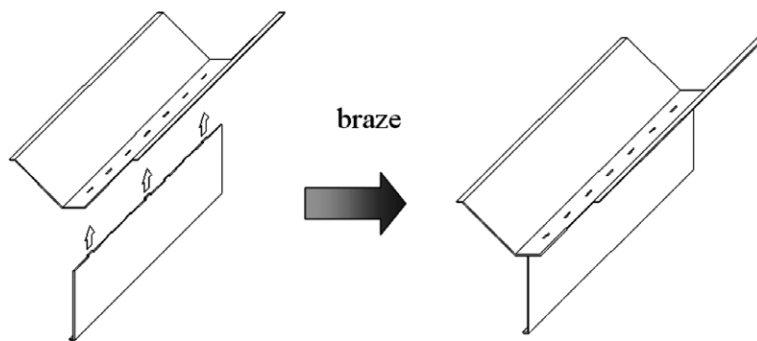


Fig. 2. Manufacture of the Y-frame sandwich cores.

P10 (wt%) braze was applied uniformly over the sheets and, upon placing the assembly into a furnace at 1120 °C in dry argon at 0.03–0.1 mbar, capillary action drew the braze into the joint.

The Y-frame specimens were manufactured by a folding and slotting technique, see Rubino et al. (2006) for details. First, the stainless steel sheets were CNC folded to form the upper half of the Y-frame and slits were laser-cut into the web as shown in Fig. 2. Next, the leg of the Y-frame was CNC folded and keys were laser machined so that the leg slotted into the slits of the upper half of the Y-frame. The assembled Y-frame and the face-sheets were then brazed together using the brazing procedure as described above. Large sandwich sheets comprising numerous corrugations or Y-frames were manufactured and were then partitioned into test specimens comprising either two corrugations or two Y-frames (as sketched in Fig. 1) by electro-discharge machining (EDM). Photographs of representative as-manufactured corrugated and Y-frame specimens are shown in Figs. 3a and b, respectively.

2.2. Material properties

The uniaxial tensile response of the AISI 304 stainless steel used to manufacture the specimens was measured at a nominal strain rate of 10^{-3} s^{-1} , and the true tensile stress versus logarithmic strain curve is plotted in Fig. 4a. This material was tested in the “as-brazed” condition to match that of the manufactured specimens. The measured 0.2% offset yield strength σ_Y and ultimate tensile strength σ_{UTS} were 200 and

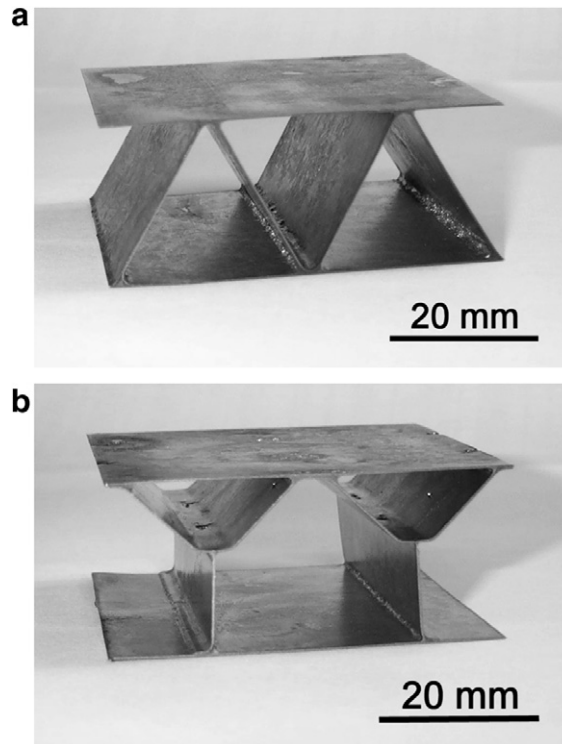


Fig. 3. Photographs of the manufactured (a) corrugated and (b) Y-frame core specimens.

700 MPa, respectively. The transition from elastic to plastic behaviour is shown in the inset. Post yield, the stainless steel exhibits an approximately linear hardening response with a tangent hardening modulus of $E_t \approx 1.4$ GPa.

Stout and Follansbee (1986) have investigated the strain-rate sensitivity of the AISI 304 stainless steel at strain-rates in the range $10^{-4} \text{ s}^{-1} < \dot{\epsilon} < 10^4 \text{ s}^{-1}$. Their data are shown in Fig. 4b, where the dynamic strength enhancement ratio R is plotted against the plastic strain-rate $\dot{\epsilon}^p$ for $10^{-3} \text{ s}^{-1} < \dot{\epsilon}^p < 10^4 \text{ s}^{-1}$. Here, R is the ratio of tensile stress $\sigma_d(\dot{\epsilon}^p = 0.1)$ at an applied strain-rate $\dot{\epsilon}^p$ to the stress $\sigma_0(\dot{\epsilon}^p = 0.1)$ at an applied $\dot{\epsilon}^p = 10^{-3} \text{ s}^{-1}$. The measured stress versus strain histories presented in Stout and Follansbee (1986) indicate that the R is reasonably independent of the level of plastic strain ϵ^p . Thus, the dynamic strength σ_d versus plastic strain ϵ^p history at a strain rate $\dot{\epsilon}^p$ can be taken as

$$\sigma_d(\dot{\epsilon}^p) = R(\dot{\epsilon}^p)\sigma_0(\epsilon^p), \quad (1)$$

where $R(\dot{\epsilon}^p)$ is given in Fig. 4b. As an example, the estimated true tensile stress versus logarithmic histories of the AISI 304 stainless steel at three selected additional values of applied strain-rate are included in Fig. 4a.

2.3. Quasi-static response

The quasi-static compressive responses of the corrugated and Y-frame sandwich cores were measured in a screw-driven test machine at an applied velocity $v_o = 0.022 \text{ mm s}^{-1}$ giving a nominal strain rate of $\dot{\epsilon} \equiv v_o/H = 10^{-3} \text{ s}^{-1}$. A laser extensometer was employed to measure the average compressive strain ϵ while the stress σ was inferred from the measurements of the applied load from the load cell of the test machine.

The measured out-of-plane quasi-static compressive responses of the corrugated and Y-frame core are plotted in Fig. 5. Both the corrugated and Y-frame cores display a peak strength (with the corrugated core having a slightly higher peak strength) followed by rapidly softening response due to the buckling of the constituent struts. Hardening is induced by core densification and commences at strains $\epsilon_D \approx 0.4$ and 0.7 for the corru-

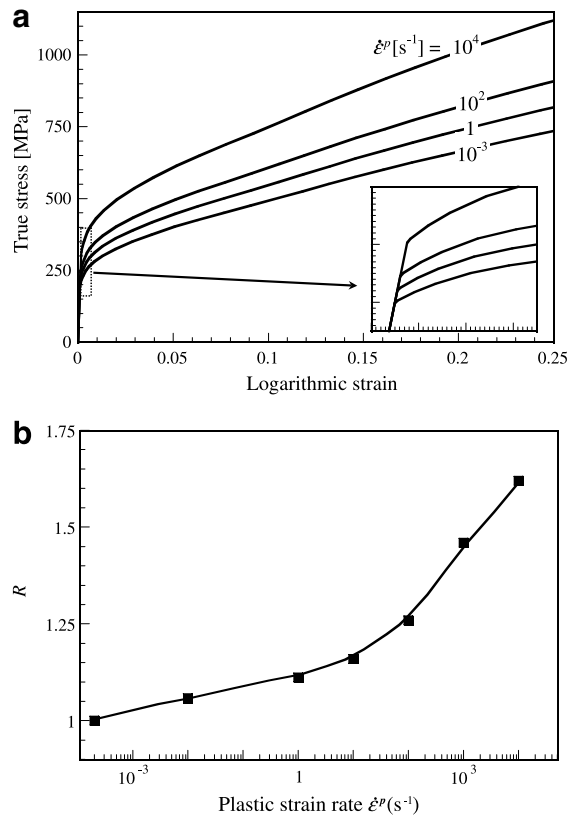


Fig. 4. (a) The measured quasi-static ($\dot{\epsilon}^p = 10^{-3} \text{ s}^{-1}$) tensile stress versus strain response of the AISI 304 stainless steel and the estimated high strain rate response at three additional values of the applied strain rate using the data of Stout and Follansbee (1986). The transition from elastic to plastic behaviour is shown inset. (b) The dynamic strength enhancement ratio R as a function of plastic strain-rate $\dot{\epsilon}^p$ for the AISI 304 stainless steel at a plastic strain $\epsilon^p = 0.1$.

gated and Y-frame cores, respectively. Photographs of the corrugated and Y-frames at selected values of the applied compressive strain ϵ are shown in Fig. 6. The struts of the corrugated core buckle as “built-in” Euler struts while the buckling mode of the Y-frame involves rotation of the node connecting the upper half of the Y-frame to the Y-frame leg. A simple strength of materials calculation of the stresses in the constituent struts at the peak stress indicate that elastic rather than plastic buckling of the constituent struts is the operative collapse mechanism for both sandwich cores. Later in this paper, the quasi-static buckling modes will be contrasted with the observed dynamic buckling modes.

2.4. Dynamic test protocol

The dynamic out-of-plane compressive responses of the corrugated and Y-frame cores were measured via direct impact tests in which the forces were measured using a strain-gauged Kolsky bar (Dharan and Hauser, 1970). Two types of tests were conducted to measure the forces or stresses on the impacted and distal ends of the specimens, referred to subsequently as the front and rear faces. Here we briefly describe the tests; readers are referred to Radford et al. (2005) for further details including the calibration procedure.

In the front face configuration (Fig. 7a), the test specimen is attached to one end of the striker bar (sometimes known as the backing mass (Harrigan et al., 1999)) and the assembly of the striker bar and specimen are projected from a gas gun so that the specimen impacts the Kolsky bar normally and centrally. Alternatively, in the rear face configuration (Fig. 7b), the specimen is placed centrally on the stationary Kolsky bar and the

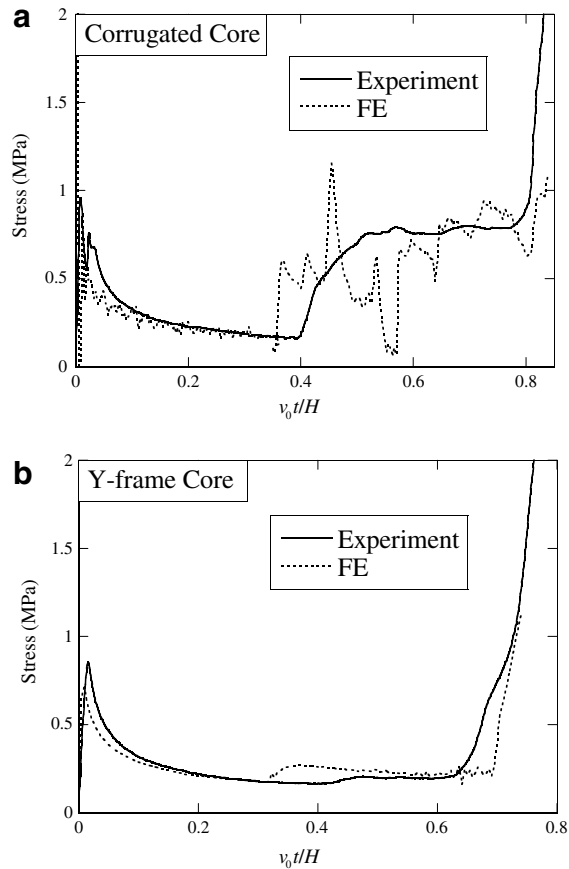


Fig. 5. The measured and FE predictions of the quasi-static compressive stress versus strain response of the corrugated and Y-frame sandwich core specimens. The relative approach velocity of the plates was $v_0 = 0.022 \text{ mm s}^{-1}$.

striker is projected so as to impact the front face of the specimen. The stress (or force) at both the impact and distal faces of the specimen are thereby measured from two separate tests.

The kinetic energy of the striker bar governs the level of compression attained and the compression velocity over the deformation period of the specimen. We aimed to attain approximately constant velocity compression and chose the striker masses accordingly. For experiments performed at velocities $v_0 < 50 \text{ ms}^{-1}$, strikers of mass $M = 6.16 \text{ kg}$ were employed while, for velocities $v_0 \geq 50 \text{ ms}^{-1}$, a 0.6 kg mass sufficed. High speed photography confirmed that the velocity of the striker remained approximately constant for compressive strains of up to 50%.

The striker was given the required velocity from approximately 2 to 200 ms^{-1} by firing it from a gas gun of barrel length 4.5 m and diameter 76.2 mm . No sabot was employed as the cylindrical striker had a clearance fit to the barrel. The bursting of copper shim diaphragms formed the breech mechanism of the gun. Laser-velocity gates were used to measure the velocity of the projectile at the exit of the gun barrel. The impacted end of the Kolsky bar was placed 100 mm from the end of the gun barrel.

The set-up of the Kolsky pressure bar is standard. A circular cylindrical bar of length 2.5 m and diameter 76.2 mm was made from Dural (aluminum alloy with yield strength 300 MPa). The contact pressure history on the impacted end of the bar was measured via diametrically opposite strain gauges placed approximately 10 diameters from the impact end of the bar; in this essentially one-dimensional impact situation, dispersion effects due to 3D elastic wave propagation effects are negligible as confirmed via a series of calibration tests by Radford et al. (2006). The elastic strain histories in the bars were monitored using two 120Ω TML foil gauges of length 1 mm in a half-Wheatstone bridge configuration. A strain bridge amplifier of cut-off frequency 500 kHz was used to provide the bridge input voltage and a digital storage oscilloscope was used to

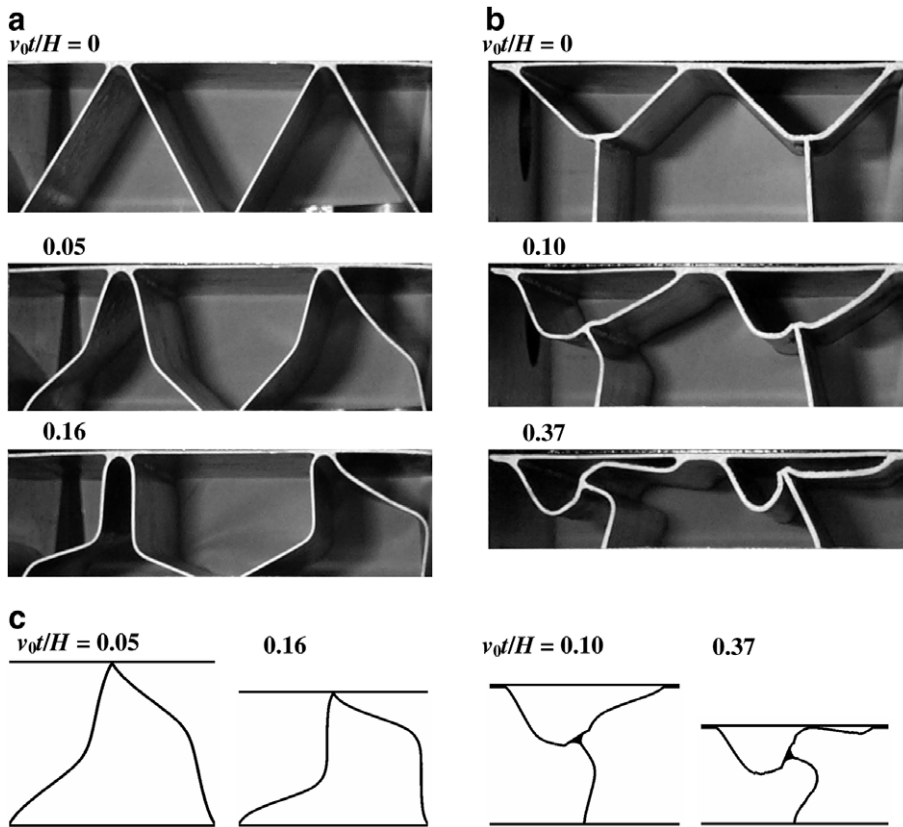


Fig. 6. A comparison between the observed and FE predictions of the quasi-static deformation mode of the (a) corrugated and (b) Y-frame sandwich core specimens. The observed deformed profiles are shown at selected values of the nominal compressive strain ϵ along with the corresponding FE predictions in (c).

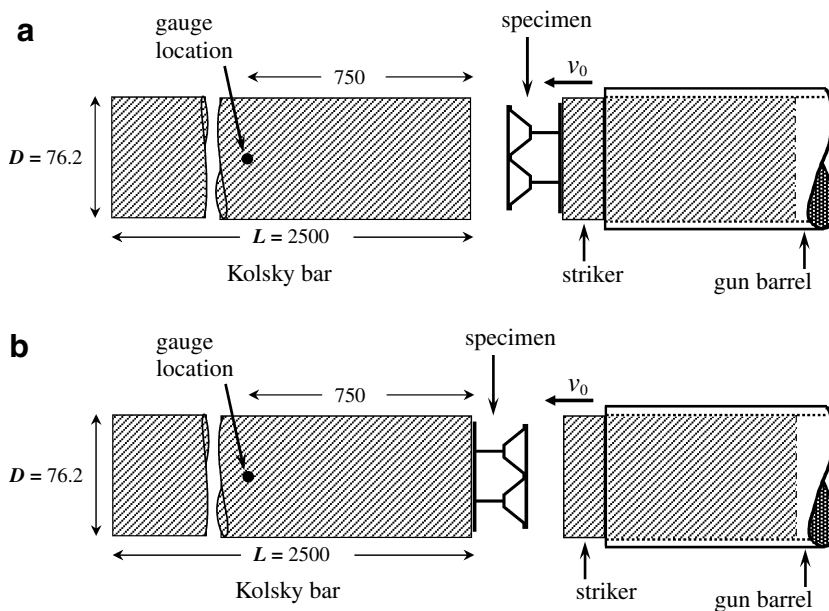


Fig. 7. Sketches of direct impact Kolsky bar setups for measuring the dynamic stress versus time histories in the (a) front face and (b) rear face configurations. All dimensions are in millimeters.

record the output. The bridge system was calibrated dynamically over the range of strains measured during the experiments and was determined to be accurate to within 3%. The longitudinal elastic wave speed was measured to be 5100 ms^{-1} , giving a time-window of $\sim 700 \mu\text{s}$ before elastic reflections from the distal end of the bar complicate the measurement of pressure.

The response time and accuracy of the measurement system were gauged from a series of calibration tests as described by Radford et al. (2005). In particular, the measurement system had a response time of approximately $10\text{--}15 \mu\text{s}$. This rise time limits the measurement of the dynamic response of the sandwich cores, especially at the higher velocities when significant compression of the specimen occurs within the response time of the measurement system.

2.5. Experimental results for the dynamic compression of the corrugated and Y-frame cores

We first present the dynamic compression measurements for the corrugated core and then contrast these results with measurements for the Y-frame sandwich core.

2.5.1. Corrugated sandwich core

The measured front and rear face stress versus normalized time $\bar{t} \equiv v_o t/H$ histories for the corrugated core specimens are presented in Figs. 8a,b, 9a,b, and 10a,b for impact velocities $v_o = 10, 56$ and 100 ms^{-1} , respectively. Time t is measured from the instant of the impact and thus the normalised time \bar{t} is a measure of the nominal compressive strain of the specimens, assuming compression at a uniform velocity v_o . FE simulations and high speed photography (presented subsequently) verified that negligible ($<1\%$) variation in velocity occurred prior to full densification. In these figures, the front and rear face stresses are defined from the measured front face force F_f and rear face force F_b as

$$\sigma_f \equiv \frac{F_f}{A_o}, \quad (2)$$

and

$$\sigma_b \equiv \frac{F_b}{A_o}, \quad (3)$$

respectively, where $A_o \equiv W \times b = 52 \times 54 \text{ mm}^2$ is the cross sectional area of the corrugated core specimens. The associated high-speed photographic sequences of the deformation of the specimens in the rear face configuration are included in Figs. 8c, 9c and 10c at inter-frame times of 100, 40 and $20 \mu\text{s}$, respectively. In each case, the exposure time of each photograph is 20% of the inter-frame time. These measurements show two distinct regimes of behaviour:

(i) $v_o \leq 30 \text{ ms}^{-1}$. The measured front and rear face stresses are approximately equal over almost the entire deformation history. Similar to the quasi-static case, the corrugated core specimens have a distinct peak in their compressive response. However, the peak stress increases with impact velocity. For example, the peak stress is seven times the quasi-static value for $v_o = 10 \text{ ms}^{-1}$. This increase in peak forces is due to dynamic stabilization against buckling as seen from the photographs in Fig. 8c. The buckling wavelength decreases with increasing velocity; compare Figs. 6a and 8c. The higher order buckling modes are associated with increased compression of the struts of the corrugated core prior to buckling, and thereby to an increase in the peak stress.

(ii) $v_o > 30.0 \text{ ms}^{-1}$. The peak stresses measured on the front face exceed those on the rear face. This indicates that the specimen is not in axial equilibrium, with wave propagation effects playing a dominant role. This is also supported by the high-speed photographs (Figs. 9c and 10c): in the initial stages of the compression, deformation of the specimens is concentrated near the impacted end, with the distal end of the specimens undergoing only small plastic deformations. For example, we observe that at $t = 40$ and $25 \mu\text{s}$ for the $v_o = 56$ and 100 ms^{-1} cases, respectively, the struts at the impacted end of the specimen have been flattened against the impacted face while the distal end of the specimen seems to be in an elastic state. Subsequently, struts buckle over their entire length, albeit at wavelengths which are much smaller than the quasi-static mode seen in Fig. 6a.

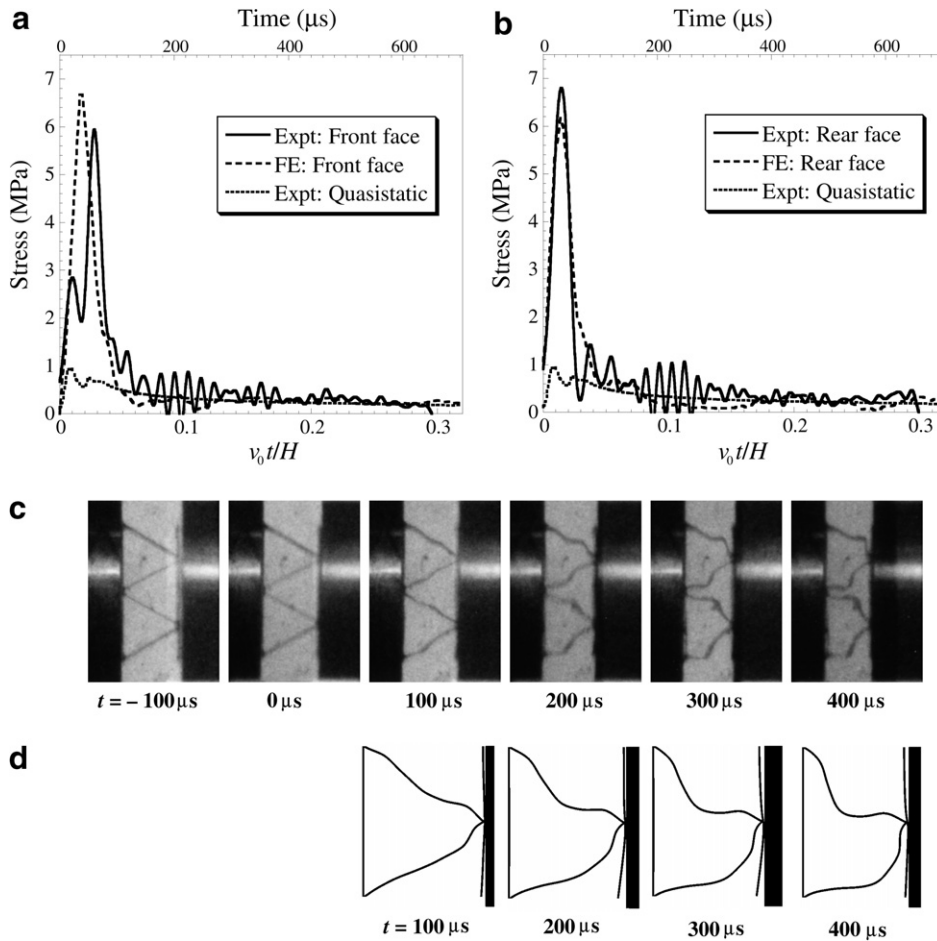


Fig. 8. The measured and FE predictions of the (a) front and (b) rear face stress versus normalised time for corrugated core specimens impacted at $v_0 = 10 \text{ ms}^{-1}$. (c) High speed photographic sequence of the deformation in the front face configuration at an inter-frame time of $100 \mu s$, and (d) corresponding FE predictions of the deformation modes.

2.5.2. Y-frame sandwich core

The measured compressive front and rear face stresses of the Y-frame sandwich core at impact velocities $v_0 = 10, 50$ and 100 ms^{-1} are plotted in Figs. 11a,b, 12a,b and 13a,b, respectively. The associated high-speed photographic sequences of the deformation are shown in Figs. 11c, 12c and 13c, respectively. Note that the Y-frame is asymmetric and here we define the front face of the Y-frame core as the face adjacent to the upper half of the Y-frame while the rear face is attached to the leg.

Similar to the corrugated core, the front and rear face stresses on the Y-frame sandwich cores are approximately equal at $v_0 = 10 \text{ ms}^{-1}$. However, unlike the corrugated core, the deformation mode of the Y-frame sandwich core at $v_0 = 10 \text{ ms}^{-1}$ dynamic compression is reasonably similar to the quasi-static mode (compare Figs. 6b and 11c). The measured peak stress of the Y-frame core at $v_0 = 10 \text{ ms}^{-1}$ is only a factor of four greater than the corresponding quasi-static value while the corresponding ratio in the corrugated core is about six. We note that the Y-frame is a bending-governed Type I structure in the notation of Calladine and English (2004) and thus is expected to be less inertia sensitive than the stretching-governed Type II corrugated core. We anticipate that decreasing the size of the web connecting the upper half of the Y-frame to the leg will transform the Y-frame to a stretching-governed Type II and thereby increase its inertia sensitivity.

At the higher impact velocities of $v_0 = 50$ and 100 ms^{-1} , the deformation modes are distinctly different from the quasi-static mode with the upper half (i.e. impacted side) of the Y-frame nearly completely crushing before deformation of the leg commences. This is reminiscent of shock type behaviour and, consistent with this observation, the measured front face stresses exceed the rear face stresses.

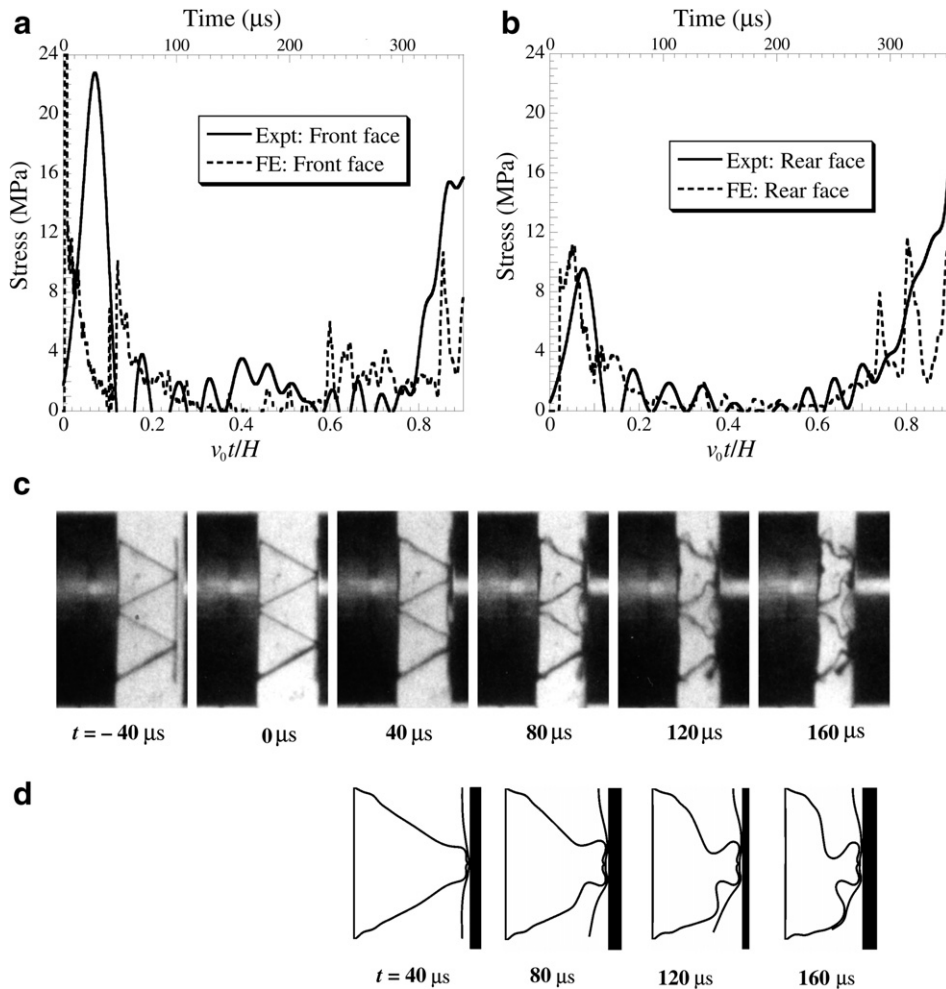


Fig. 9. The measured and FE predictions of the (a) front and (b) rear face stress versus normalised time for corrugated core specimens impacted at $v_0 = 56 \text{ ms}^{-1}$. (c) High speed photographic sequence of the deformation in the front face configuration at an inter-frame time of $40 \mu\text{s}$, and (d) corresponding FE predictions of the deformation modes.

3. Finite element study

A limited finite element (FE) investigation of the dynamic compression of the corrugated and Y-frame core specimens has been performed. The aims of this investigation are:

- (i) to determine the accuracy of two-dimensional finite element calculations in predicting the dynamic compressive response of these cores;
- (ii) to use the finite element calculations to assess the effect of the face-sheet on the measured core response; and
- (iii) to understand the underlying dynamic strengthening mechanisms and to investigate the effect of specimen size on the dynamic core behaviour.

3.1. Two-dimensional FE simulations

All computations were performed using the explicit time integration version of the commercially available FE code ABAQUS (version 6.5). The geometries of the structures (including the face-sheets) were identical to

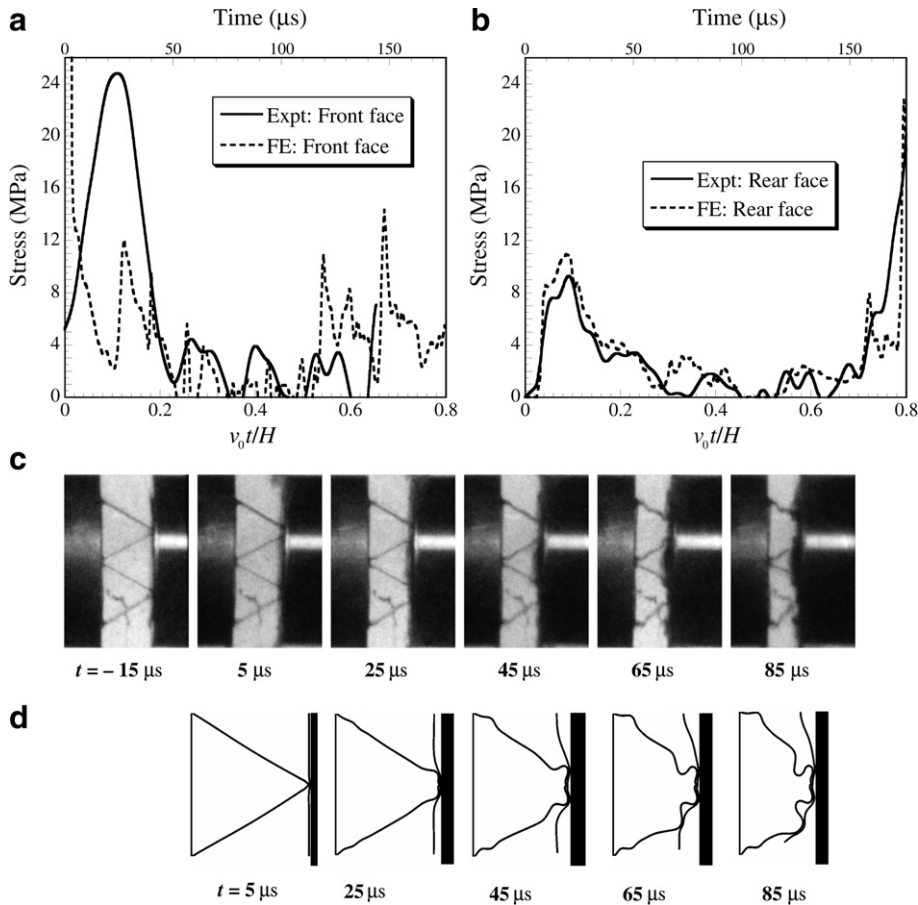


Fig. 10. The measured and FE predictions of the (a) front and (b) rear face stress versus normalised time for corrugated core specimens impacted at $v_0 = 100 \text{ ms}^{-1}$. (c) High speed photographic sequence of the deformation in the front face configuration at an inter-frame time of $20 \mu\text{s}$, and (d) corresponding FE predictions of the deformation modes.

those employed in the experimental investigation (Fig. 1) and were modelled using four-noded plane strain quadrilateral elements with reduced integration (type CPE4R in ABAQUS notation).

A mesh with approximately square elements of size $t/8$, where t is the web-thickness, was employed in all calculations. Mesh sensitivity studies revealed that additional mesh refinements did not improve the accuracy of the calculations appreciably. Perfect bonding between core and face-sheets is assumed in all cases. The ABAQUS “surface-to-surface contact” and “self-contact” options were used to enforce a hard contact between all potentially contacting surfaces.

3.1.1. Material properties

The specimens comprised AISI 304 stainless steel sheets. Unless otherwise specified, the stainless steel was modelled as J2-flow theory rate-dependent solid of density $\rho = 8000 \text{ kgm}^{-3}$, Young’s modulus $E = 210 \text{ GPa}$ and Poisson ratio $\nu = 0.3$. The uniaxial tensile true stress versus equivalent plastic strain curves at plastic strain-rates $10^{-3} \text{ s}^{-1} \leq \dot{\epsilon}^p \leq 10^4 \text{ s}^{-1}$ were tabulated in ABAQUS using the prescription described in Section 2.2 and employing the data of Fig. 4. The transition from elastic to plastic behaviour is shown in the inset. Predictions of the onset of plastic buckling are expected to be sensitive to this transition, hence the measured stress versus strain curves (Fig. 4a) were used in the simulations rather than empirical fits such as the Johnson-Cook model.

There exists an accumulation of braze at the joint of the upper half of the Y-frame and the Y-frame leg, and this is depicted by the butt-joint in Fig. 1b. The material in this butt-brazed joint was assumed to be elastic-

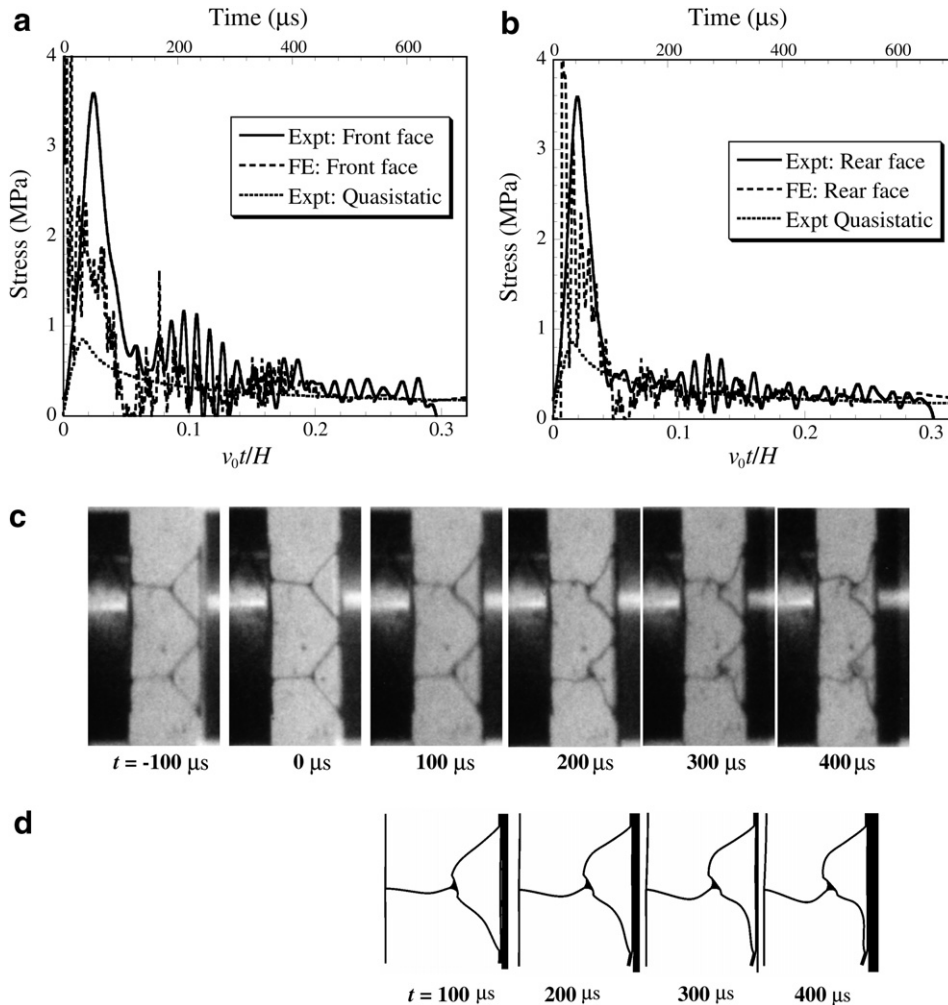


Fig. 11. The measured and FE predictions of the (a) front and (b) rear face stress versus normalised time for Y-frame sandwich core specimens impacted at $v_0 = 10 \text{ ms}^{-1}$. (c) High speed photographic sequence of the deformation in the front face configuration at an inter-frame time of $100 \mu\text{s}$, and (d) corresponding FE predictions of the deformation modes.

ideally plastic with a Young's modulus $E = 210 \text{ GPa}$, Poisson ratio $\nu = 0.3$ and yield strength $\sigma_Y = 800 \text{ MPa}$ consistent with the fact that the braze alloy is significantly harder than the stainless steel (Côté et al., 2006). The strain-rate sensitivity of the braze alloy was neglected and it was modelled as a rate-independent J2-flow theory solid.

3.1.2. Geometric imperfections

A close examination of the Y-frame and corrugated core specimens revealed that geometric imperfections with an amplitude on the order of the sheet thickness were present in the as-manufactured samples. Following Radford et al. (2006), geometric imperfections in the form of the first static eigenmode of elastic buckling were introduced in the FE geometries of the corrugated and Y-frame cores. In performing these eigenmode calculations, the face-sheets were included so that imperfections were introduced in both the core and the face-sheets. Consistent with the imperfections observed in the manufactured specimens (Fig. 3), the maximum amplitude of the imperfections was set equal to the sheet thickness t in all calculations reported subsequently. We note that, similar to the findings of Radford et al. (2006), the dynamic stress versus time response of these sandwich cores is not sensitive to the precise nature of the imperfections employed, though of course the exact shape of the buckling mode varies with the choice of imperfection.

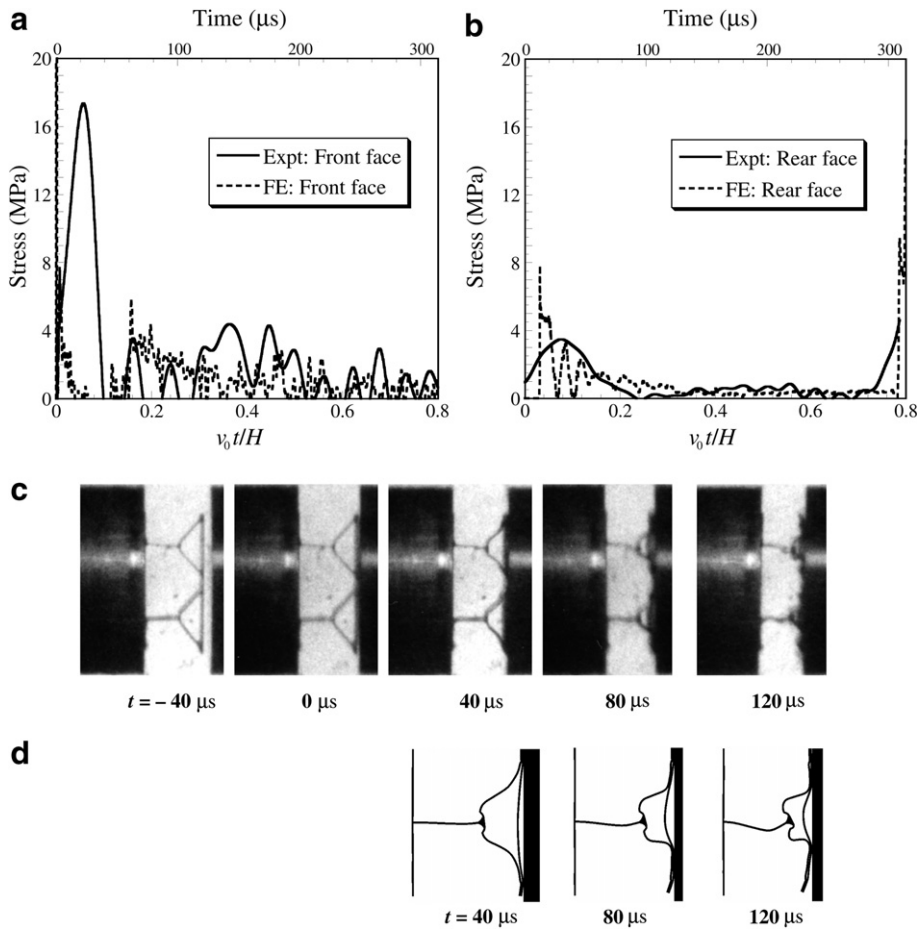


Fig. 12. The measured and FE predictions of the (a) front and (b) rear face stress versus normalised time for Y-frame sandwich core specimens impacted at $v_0 = 56 \text{ ms}^{-1}$. (c) High speed photographic sequence of the deformation in the front face configuration at an inter-frame time of $40 \mu\text{s}$, and (d) corresponding FE predictions of the deformation modes.

No imperfections in terms of material properties and other manufacturing defects were introduced into the model: we shall show subsequently, that simple geometric imperfections were adequate to capture the measured behaviour. Moreover, the high temperature brazing process annealed the specimens and thus residual stresses are expected to be negligible in the specimens and thus residual stress effects are ignored in the FE model.

3.1.3. Loading and boundary conditions

A single unit of each core was analysed, i.e. a single corrugation comprising two inclined struts of the corrugated core and a single unit of the Y-frame. Two types of simulations were performed: impact simulations and constant velocity compression of the core. The boundary conditions employed in these two types of simulations are illustrated in Fig. 14.

(a) *Impact simulations:* The impact event of the striker was simulated by modelling the entire striker bar as shown in Fig. 14a. The striker is given an initial axial velocity v_0 and impacts the front face of the sandwich core specimen while the back of the rear face has frictionless contact with a rigid foundation. Circular cylindrical steel strikers were employed in the experiments. However, in the 2D simulations, the striker was modelled as rectangular bar of width $W/2$ and depth $b = 54 \text{ mm}$. The striker was treated as a linear elastic solid of Young's modulus $E = 210 \text{ GPa}$, Poisson ratio $\nu = 0.3$ and density $\rho_f = 8000 \text{ kgm}^{-3}$. The length of the striker was adjusted so the striker mass was the same as that employed in the experiments (i.e. $M = 6.16$ or 0.6 kg

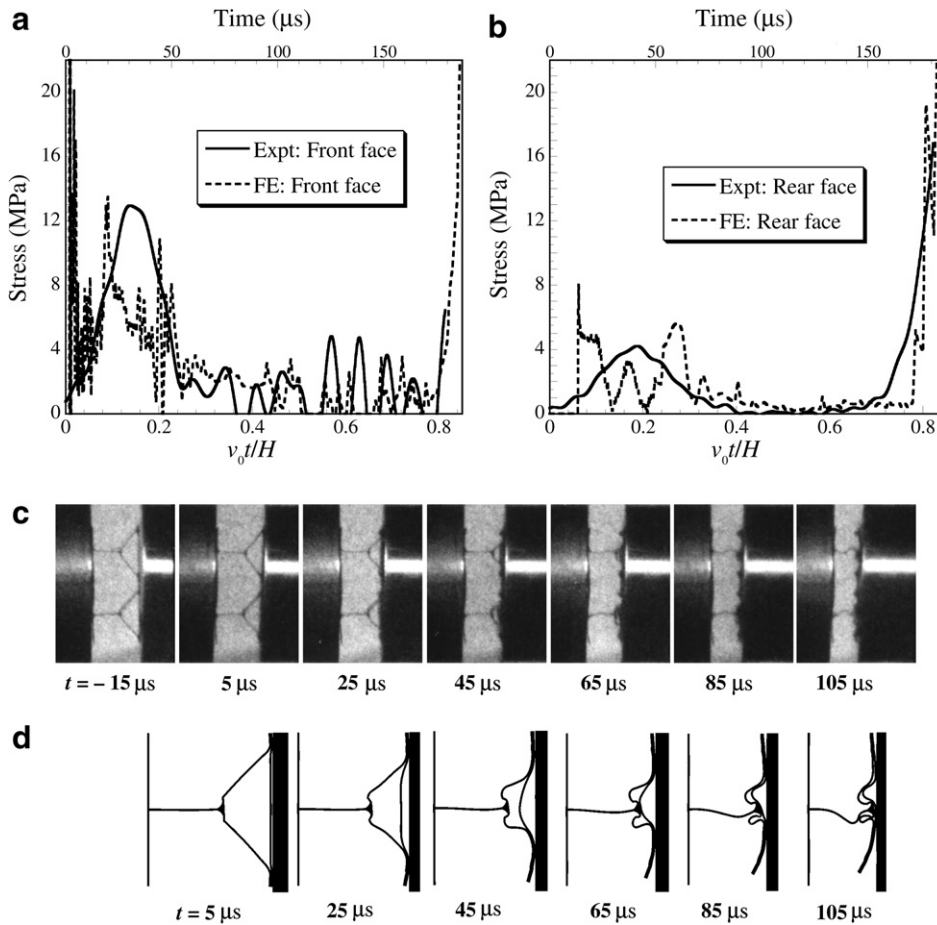


Fig. 13. The measured and FE predictions of the (a) front and (b) rear face stress versus normalised time for Y-frame sandwich core specimens impacted at $v_0 = 100 \text{ ms}^{-1}$. (c) High speed photographic sequence of the deformation in the front face configuration at an inter-frame time of $20 \mu\text{s}$, and (d) corresponding FE predictions of the deformation modes.

depending upon the impact velocity giving a striker length $L = M/(Wb)$. The striker was represented by plane strain elements (CPE4R in the ABAQUS notation), constrained to move only in the axial direction and given an initial velocity v_0 . Contact between the striker and the front face-sheet of the sandwich was modelled using the hard frictionless contact option in ABAQUS. The axial forces on the front and rear face-sheet were monitored as functions of time by integrating contact pressures across the front face/striker interface and back side of rear face, respectively.

(b) *Constant velocity compression of the cores:* In order to determine the intrinsic core behaviour, we also performed simulations where the face-sheets were modelled as rigid bodies and the core was compressed at a constant rate by imposing a constant axial velocity v_0 on the front-face sheet with the rear face-sheet fully constrained, i.e. no deformation of the face sheets was permitted. This is illustrated in Fig. 14b for the Y-frame core. The axial forces on the front and rear faces were monitored as a function of time to determine the front and rear face stress versus time history. These boundary conditions were also used to obtain the FE predictions of the quasi-static responses of the core with $v_0 = 0.022 \text{ mms}^{-1}$.

3.2. Comparison of measurements and FE predictions using impact boundary conditions

A comparison of the measured and FE predictions of the quasi-static stress versus strain response of the corrugated and Y-frame cores is presented in Fig. 5, while the deformation modes are compared in Fig. 6.

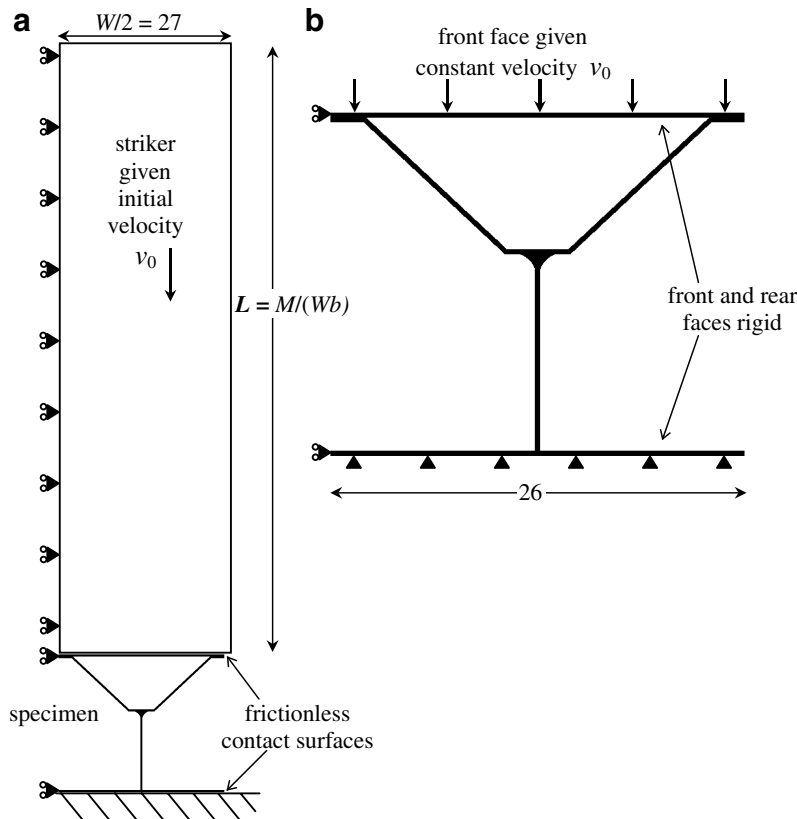


Fig. 14. Configurations for FE simulations showing boundary conditions, for Y-frame core specimens. (a) Striker and specimen for impact simulations. (b) Specimen for constant velocity crushing simulations. All dimensions are in mm. Equivalent set-ups used for corrugated core specimens.

The FE predictions of both the deformation modes and stress versus strain histories are in good agreement throughout the collapse response.

The measured and predicted dynamic compressive responses of the corrugated and Y-frame sandwich cores are compared in Figs. 8–13. The FE simulations reported in these figures were performed using the impact boundary conditions detailed above. We note that the FE simulations capture the observed deformation modes for both the corrugated and Y-frame sandwich cores over the range of impact velocities investigated. Consistent with the observations, the FE calculations predict:

- (i) A higher order buckling mode is triggered in the corrugated core for compression at $v_0 = 10 \text{ ms}^{-1}$ compared with the quasi-static response, while the deformation mode of the Y-frame core remains unchanged from the quasi-static response.
- (ii) For compression at $v_0 = 50$ and 100 ms^{-1} , initial deformation is concentrated near the impacted end for both the Y-frame and corrugated sandwich cores.

In line with the high-speed photographs of sandwich core deformation, the FE calculations predict that the front face-sheet undergoes significant bending with only a fraction of the face-sheet remaining in contact with the striker at various stages of the deformation. It is concluded that the front and rear face stress versus time histories are affected by the face-sheet deformation in the experiments as well as in the FE calculations.

While the observed and predicted deformation modes are in good agreement over the range of velocities investigated here, the FE predictions of the stress histories agree with the measurements only at low impact velocities ($v_0 = 10 \text{ ms}^{-1}$); compare Figs. 8a and 11a. At the higher impact velocities, there is reasonable agreement between the measured and predicted rear face stress versus time histories, however there are major

discrepancies between the measurements and predictions of the front face stress versus time histories. In particular, (i) the measured peak stresses occur at $t \approx 20 \mu\text{s}$ while the FE calculations predict that the front face stress peaks at $t \approx 2 \mu\text{s}$ and (ii) the peak stresses in the FE calculations are significantly higher than the measured peak stresses. These discrepancies between the measurements and predictions of the front face stresses can be rationalized as follows. In the experiments, impact of the specimen against the stationary direct impact Kolsky bar results in the $t = 0.3 \text{ mm}$ front face-sheet being brought to rest on a timescale of a few microseconds. This arrest gives rise to a short duration stress pulse with a high peak force as captured by the FE calculations. However, the response time of the measurement apparatus is about $15 \mu\text{s}$ and thus the experiments

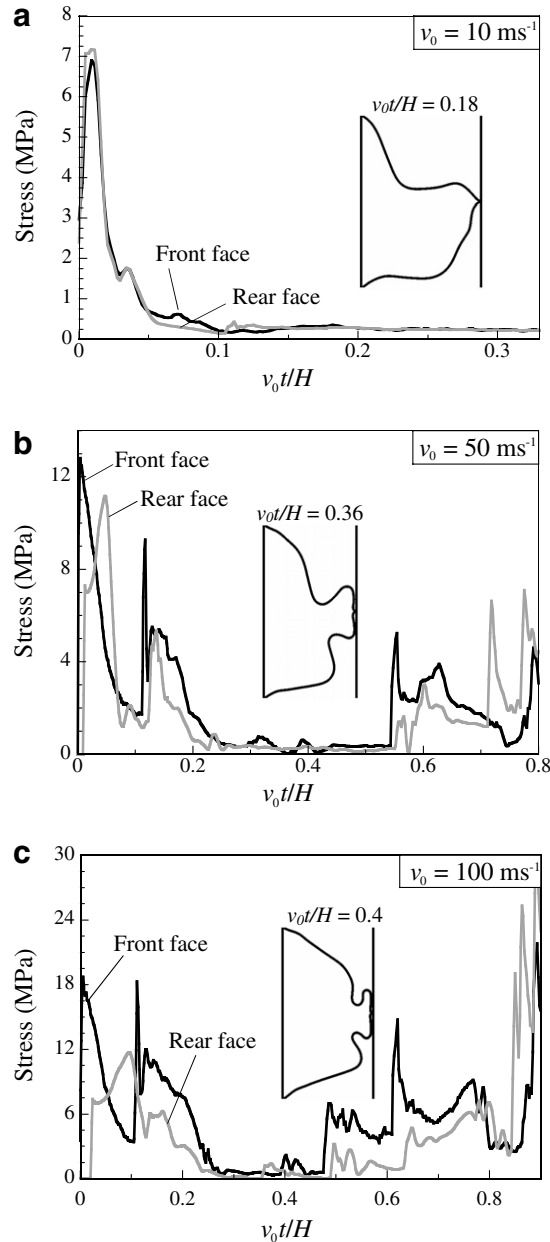


Fig. 15. Constant velocity FE predictions of the front and rear face stress versus normalised time histories of the corrugated sandwich core. (a) $v_0 = 10 \text{ ms}^{-1}$, (b) $v_0 = 50 \text{ ms}^{-1}$ and (c) $v_0 = 100 \text{ ms}^{-1}$. The predicted deformed profiles at selected values of nominal strain are included as inserts in the figures.

are unable to capture this initial stress pulse resulting in the discrepancies between the measurements and the predictions.

These comparisons between FE predictions and measurements reveal that it is difficult to ascertain the intrinsic dynamic response of the sandwich core from the experimental measurements for two reasons:

- (i) At high impact velocities, the front face-sheet has a significant influence on the front face stress history. It is difficult in such situations to deconvolute the intrinsic dynamic core strength from the strength of the sandwich comprising face-sheet and the core.

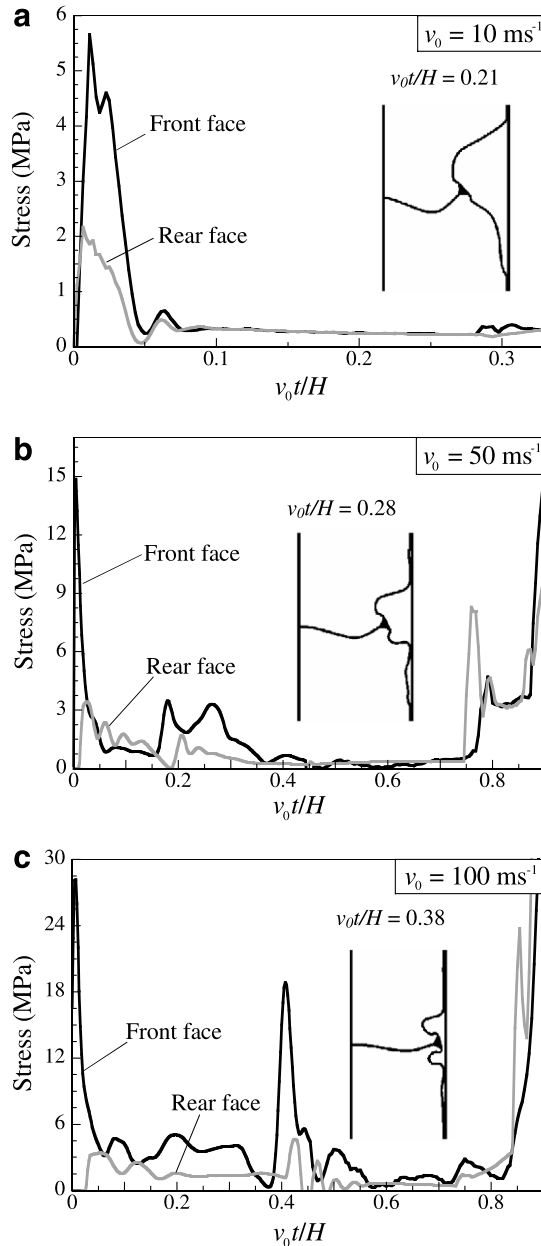


Fig. 16. Constant velocity FE predictions of the front and rear face stress versus normalised time histories of the Y-frame sandwich core. (a) $v_0 = 10 \text{ ms}^{-1}$, (b) $v_0 = 50 \text{ ms}^{-1}$ and (c) $v_0 = 100 \text{ ms}^{-1}$. The predicted deformed profiles at selected values of nominal strain are included as inserts in the figures.

- (ii) The measured response is significantly affected by the response time of the measurement apparatus. For example, for compression at $v_o = 100 \text{ ms}^{-1}$, the sandwich cores have compressed by approximately 10% ($t = 20 \text{ }\mu\text{s}$) before measurements from the direct impact Kolsky bar are deemed reliable.

3.3. Constant velocity compression of the sandwich core: FE predictions of the intrinsic dynamic properties of the core

FE predictions of the front and rear face stress versus time histories for the constant velocity compression of the corrugated and Y-frame core are presented in Figs. 15 and 16, respectively. These simulations were performed in the manner described in Section 3.1. Similar to the impact loading simulations and measurements we observe that, while the front and rear face stresses are approximately equal at $v_o = 10 \text{ ms}^{-1}$, the front face stresses exceed the rear face stresses in the early stages of compression for $v_o \geq 10$ and 50 ms^{-1} for the Y-frame and corrugated cores, respectively. However, the front face stresses in these high velocity simulations are significantly lower than those obtained in the impact simulations discussed in Section 3.2. We conclude that the front face stresses in impact simulations are dominated by the forces required to accelerate (or decelerate) the $t = 0.3 \text{ mm}$ steel front face and do not reflect the intrinsic dynamic strength of the core. In contrast,

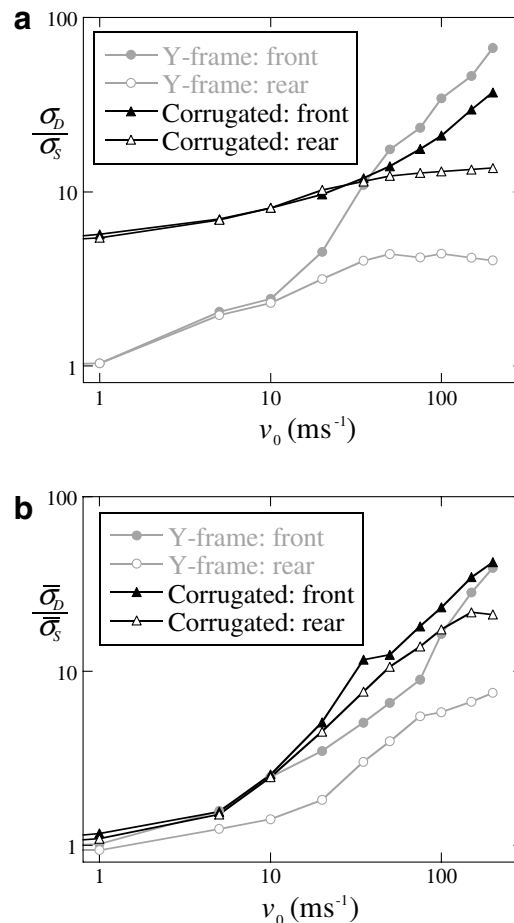


Fig. 17. FE predictions of the dynamic (a) peak stress σ_D and (b) the average stress $\bar{\sigma}_D$ of the corrugated and Y-frame sandwich cores as a function of the constant compression velocity v_o . Both the front and rear face stresses are included and the dynamic stresses are normalised by the corresponding quasi-static peak and average stresses, σ_s and $\bar{\sigma}_s$, obtained from the experimental results in Fig. 5.

the constant velocity compression simulations reported here are unaffected by the face-sheet properties and directly give the dynamic response of the core.

The constant velocity FE predictions of the deformed profiles of the core are included in Figs. 15 and 16 at selected values of the compressive strain $v_0 t/H$. A comparison with the FE predictions and observations of the deformation modes in Figs. 8–13 suggests that the deformation modes are approximately the same in both the impact and constant applied velocity loading situations. Taken together, the results presented here and in Section 3.2 suggest that the experiments are adequate to determine the dynamic buckling modes of the cores. However, we are unable to measure the high velocity dynamic front face stresses exerted by the cores as the measurements are (i) significantly affected by the face sheet deformation, and (ii) the response time of the measurement apparatus is too slow to enable high fidelity measurements.

We have shown above that the FE calculations predict the dynamic core response with sufficient accuracy (both in terms of the deformation modes and rear face stress versus time histories). We now proceed to determine the “intrinsic” dynamic response of the core by conducting a series of constant velocity FE calculations. The FE predictions of the sensitivity of the peak stress σ_D and average stress $\bar{\sigma}_D$ to velocity are plotted in Figs. 17a and b, respectively. Both the front and rear face stress predictions are included in Fig. 17, and $\bar{\sigma}_D$ is defined as $\bar{\sigma}_D \equiv 5.0 \int_0^{0.2} \sigma d(v_0 t/H)$ where σ is either the rear or front-face stress σ_b or σ_f , respectively. Thus, $\bar{\sigma}_D$ is the average stress over 20% nominal core compression, i.e. the average stress from $v_0 t/H = 0$ to $v_0 t/H = 0.2$. The

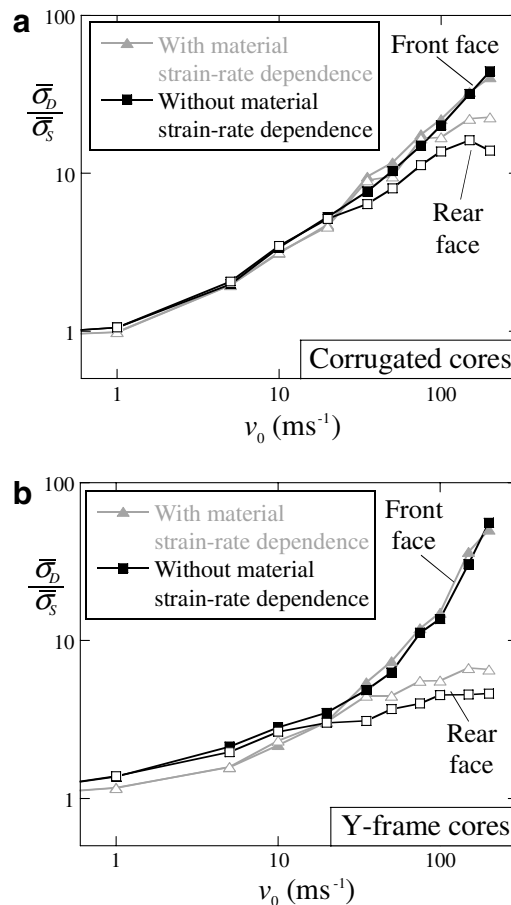


Fig. 18. FE predictions of the average dynamic stress $\bar{\sigma}_D$ of the (a) corrugated and (b) Y-frame sandwich core as a function of the constant compression velocity v_0 . The FE predictions with and without material strain rate sensitivity are plotted. Both the front and rear face stresses are included and the dynamic stresses are normalised by the corresponding average quasi-static stress $\bar{\sigma}_s$ obtained from the experimental results in Fig. 5.

stresses in Fig. 17 are normalized by the quasi-static values of the peak stress σ_S and average stress $\bar{\sigma}_S$ from experimental results plotted in Fig. 5. Certain similarities and differences between the corrugated and Y-frame cores emerge from the peak stress comparisons in Fig. 17a.

- (i) The front face stresses increase with increased velocity for both the sandwich cores over the range of compression velocities investigated here. In contrast, the rear face stresses increase with increasing velocity for $v_o \leq 30 \text{ ms}^{-1}$ and show negligible sensitivity to v_o at higher velocities. This velocity sensitivity at relatively low compression velocities is due to inertial stabilisation against elastic buckling of the Y-frame and corrugated sandwich cores. The Y-frame is a bending-governed structure while the corrugated core is a stretching-governed structure (Types I and II, respectively in the notation of Calladine and English (2004)). Consistent with expectations, the Y-frame is less inertia-sensitive than the corrugated core.
- (ii) The front and rear face stresses are approximately equal for $v_o \leq 30 \text{ ms}^{-1}$ and $v_o \leq 60 \text{ ms}^{-1}$ for the Y-frame and corrugated cores, respectively. Plastic wave effects in the cores become significant at higher velocities with the front face stresses exceeding the rear face stresses. These wave effects become significant at lower velocities in the Y-frame core as the asymmetry of the core implies that a larger fraction of the core mass is adjacent to the front face in the Y-frame core compared to the corrugated core.

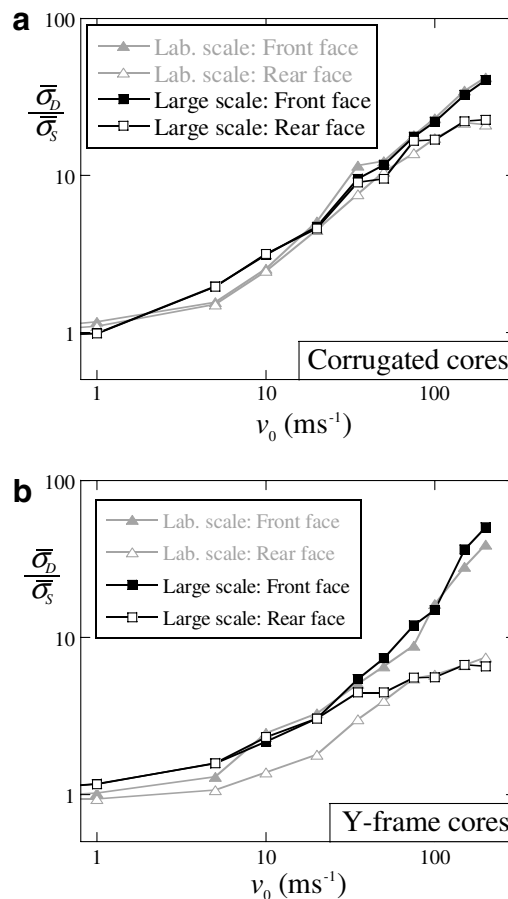


Fig. 19. FE predictions of the average dynamic stress $\bar{\sigma}_D$ of the (a) corrugated and (b) Y-frame sandwich core as a function of the constant compression velocity v_o . The FE predictions for the laboratory scale and a large scale (geometrically self-similar to the laboratory specimens but a factor of 10 larger) sandwich cores are plotted. Both the front and rear face stresses are included and the dynamic stresses are normalised by the corresponding average quasi-static stress $\bar{\sigma}_S$ obtained from the experimental results in Fig. 5.

The average dynamic stresses $\bar{\sigma}_D$ of the two cores display a significantly lower velocity sensitivity especially in the lower velocity range ($v_o < 10 \text{ ms}^{-1}$) where inertia stabilization against buckling is the main contributor to the dynamic enhancement of the peak stresses. Both the corrugated and Y-frame cores typically display a sharp stress drop following the peak stress (Figs. 15 and 16, respectively) and thus, when the stress is averaged over $0 \leq v_o t/H \leq 0.2$, inertial stabilisation against buckling has a much smaller effect. Plastic wave effects are more significant in the Y-frame core with the average front face stress exceeding the average rear face stress for $v_o > 10 \text{ ms}^{-1}$ while the average front and rear face stresses are approximately equal in the corrugated core up to $v_o = 100 \text{ ms}^{-1}$.

3.4. Scaling of the dynamic stresses: effect of strain rate sensitivity and size

The corrugated and Y-frame sandwich cores are designed for application in large-scale blast-resistant marine structures, with typical core heights on the order of 0.1–1 m. The experiments and FE calculations reported above were performed on small-scale specimens. Here we investigate the scaling of the dynamic strength of the Y-frame and corrugated cores with the size of the structure in order to relate the results obtained for the laboratory-scale specimens to full-scale marine structures.

We first make explicit the relevant non-dimensional groups that govern the scaling of the dynamic response of the sandwich cores. The AISI stainless steel can be considered to be an elastic-plastic material with a Young's modulus E , Poisson's ratio ν , yield strength σ_Y and a linear hardening plastic response with plastic modulus E_t . The plastic wave speed in the material is $c_{pl} \equiv \sqrt{E_t/\rho_t}$, where ρ_t is the density of the steel. In addition, the stainless steel exhibits strain rate sensitivity: for the purposes of illustration of the relevant non-dimensional groups only it suffices to assume a linear rate sensitivity characterised by a linear viscosity η . Then, the non-dimensional groups governing the response of the sandwich core are σ_Y/E , E_t/E , $\frac{\eta}{H\rho c_{pl}}$ and the non-dimensional groups describing the core geometry (e.g. the aspect ratio t/H and corrugation angle ω for the corrugated core). In addition, the non-dimensional loading variable v_o/c_{pl} specifies the compression velocity. Recall that the width of the shock front in a material with a linear viscous rate sensitivity scales as $\eta/(\rho c_{pl})$ (Kaliski and Włodarczyk, 1967). Thus, the non-dimensional group $\frac{\eta}{H\rho c_{pl}}$ gives the ratio of the shock width to the core height and couples the solid material behaviour with the actual size of the core. If $\frac{\eta}{H\rho c_{pl}} \ll 1$, for both the laboratory-scale and full-scale sandwich cores, the strain-rate sensitivity of the 304 stainless is expected to play a negligible role, and the laboratory-scale results presented here are immediately applicable to the full-scale sandwich cores. We proceed to investigate the effect of the strain rate sensitivity of the 304 stainless steel on the FE predictions of the dynamic core response using the actual strain-rate sensitivity of the 304 stainless steel as presented in Fig. 4.

Finite element predictions of the average dynamic crushing strengths $\bar{\sigma}_D$ of the corrugated and Y-frame cores made from a rate independent material are presented in Figs. 18a and b, respectively. These constant velocity simulations were performed as described in Section 3.1 with one difference: the strain rate sensitivity of the 304 stainless steel was not considered, i.e. the 304 stainless steel was modelled as a J2-flow theory rate-independent solid with the tensile response equivalent to the quasi-static response plotted in Fig. 4a (for an applied strain rate $\dot{\epsilon} = 10^{-3} \text{ s}^{-1}$). For comparison purposes, the FE predictions of Fig. 17b, with the rate sensitivity of the 304 stainless steel considered, are also included in Fig. 18. We observe that neglect of the rate sensitivity of the 304 stainless steel has only a small effect upon the predicted dynamic stresses over the ranges of velocities considered here even though maximum strain-rates of up to 10^4 s^{-1} were predicted by the FE calculations within the plastic hinges in the cores. This suggests that the laboratory-scale specimens investigated here are sufficiently large for their dynamic compressive response to be representative of full-scale structures.

We confirm this inference by performing constant velocity FE simulations on full-scale corrugated and Y-frame sandwich cores. These simulations were performed in a manner identical to those reported in Section 3.1 (with the strain rate sensitivity of AISI 304 stainless steel included), albeit on a larger scale structure. All dimensions of the core were increased by a factor of ten while keeping the cores geometrically similar to the laboratory scale specimens. A comparison between the average dynamic strengths of the laboratory and full-scale corrugated and Y-frame sandwich cores is presented in Figs. 19a and b, respectively. In line with our expectations we observe that the response of the two sizes of sandwich cores is almost identical over the range of velocities investigated here. The results presented here confirm that the laboratory-scale experiments are adequate in illuminating the dynamic response of the full-scale sandwich cores.

Finally we note that the dynamic responses of the Y-frame and corrugated sandwich cores investigated here provide the essential information required for investigating the fluid-structure interaction in sandwich plates comprising these cores. For example, in a sandwich plate subjected to an underwater blast, the wet face rapidly accelerates to a maximum velocity, just before water cavitation commences. Thereafter, the core imposes a push back stress, causing the wet face to decelerate. Simultaneously, the back face accelerates. These rates depend on the dynamic response of the core as exemplified by Deshpande and Fleck (2005) and Hutchinson and Xue (2005): the dynamic responses investigated here directly feed into such fluid-structure interaction models; see, for example, Liang et al. (2007).

4. Concluding remarks

The dynamic out-of-plane compressive responses of stainless steel corrugated and Y-frame sandwich cores have been investigated for impact velocities ranging from quasi-static values to 200 ms^{-1} . The stresses on both the front and rear faces of the square-honeycombs were measured in the dynamic tests using a direct impact Kolsky bar. Two distinct mechanisms govern the dynamic response of the cores: (i) inertial stabilization of the webs against buckling and (ii) plastic wave effects. The front and rear face peak stresses remain approximately equal for impact velocities less than 30 and 60 ms^{-1} for the Y-frame and corrugated sandwich cores, respectively. Inertial stabilization of the webs against buckling is the dominant dynamic strengthening mechanism at these lower velocities. However, inertial stabilisation has a smaller effect on the bending-dominated Y-frame cores compared to the stretching-dominated corrugated cores. At higher impact velocities, plastic wave effects within the core members result in the front face stresses increasing with increasing velocity while the rear face stresses remain approximately constant.

Finite element calculations predict the rear face stresses and dynamic deformation modes to reasonable accuracy. However, the relatively slow response time of the measurement apparatus results in poor agreement between the measured and predicted front face stresses, especially at high impact velocities. The finite element calculations demonstrate that material strain-rate effects have a negligible effect on the dynamic compressive response of the laboratory-scale sandwich core specimens and consequently the laboratory-scale specimens tested here are adequate in revealing in the dynamic strengthening mechanisms of full-scale corrugated and Y-frame sandwich cores.

Acknowledgements

The authors are grateful to ONR for their financial support through US-ONR IFO Grant No. N00014-03-1-0283 on The Science and Design of Blast Resistant Sandwich Structures and to the Isaac Newton Trust, Trinity College Cambridge.

References

- Calladine, C.R., English, R.W., 2004. Strain-rate and inertia effects in the collapse of two types of energy-absorbing structure. *International Journal of Mechanical Sciences* 26 (11/12), 689–701.
- Côté, F., Deshpande, V.S., Fleck, N.A., Evans, A.G., 2006. The compressive and shear responses of corrugated and diamond lattice materials. *International Journal of Solids and Structures* 43, 6202–6242.
- Deshpande, V.S., Fleck, N.A., 2005. One-dimensional response of sandwich plates to underwater shock loading. *Journal of the Mechanics and Physics of Solids* 53 (11), 2347–2383.
- Dharan, C.K.H., Hauser, F.E., 1970. Testing techniques based on the split Hopkinson bar. *Experimental Mechanics* 10, 70–376.
- Ferri, E., Antinucci, E., He, M.Y., Hutchinson, J.W., Zok, F.W., Evans, A.G., 2007. Dynamic buckling of impulsively loaded prismatic cores. *Journal of the Mechanics of Materials and Structures* 1 (8), 1345.
- Fleck, N.A., Deshpande, V.S., 2004. The resistance of clamped sandwich beams to shock loading. *Journal of Applied Mechanics* 71 (3), 386–401.
- Harrigan, J.J., Reid, S.R., Peng, C., 1999. Inertia effects in impact energy absorbing materials and structures. *International Journal of Impact Engineering* 22, 955–979.
- Hutchinson, J.W., Xue, Z., 2005. Metal sandwich plates optimised for pressure pulses. *International Journal of Mechanical Sciences* 47 (4-5), 545–569.

- Kaliski, S., Włodarczyk, E., 1967. On certain closed-form solutions of the propagation and reflection problem of an elastic-visco-plastic wave in a bar. *Archiwum Mechaniki Stosowanej* 19, 433–452.
- Lee, S., Barthelat, F., Hutchinson, J.W., Espinosa, H.D., 2006. Dynamic failure of metallic pyramidal truss core materials – experiments and modelling. *International Journal of Plasticity* 22 (11), 2118–2145.
- Liang, Y., Spuskanyuk, A.V., Flores, S.E., Hayhurst, D.R., Hutchinson, J.W., McMeeking, R.M., Evans, A.G., 2007. The response of metallic sandwich panels of water blast. *Journal of Applied Mechanics* 74, 81.
- Radford, D.D., Deshpande, V.S., Fleck, N.A., 2005. The use of metal foam projectiles to simulate shock loading on a structure. *International Journal of Impact Engineering* 31 (9), 1152–1171.
- Radford, D.D., McShane, G.J., Deshpande, V.S., Fleck, N.A., 2006. Dynamic compressive response of stainless steel square-honeycombs. *Journal of Applied Mechanics* (to appear).
- Rubino, V., Deshpande, V.S., Fleck, N.A., 2006. The dynamic response of Y-frame and corrugated core sandwich beams. *International Journal of Solids and Structures* (submitted for publication).
- Stout, M.G., Follansbee, P.S., 1986. Strain-rate sensitivity, strain hardening, and yield behaviour of 304L stainless steel. *Transactions of ASME: Journal of Engineering Materials Technology* 108, 344–353.
- Vaughn, D.G., Hutchinson, J.W., 2006. Buckle waves. *European Journal of Mechanics A/Solids* 25 (1), 1–12.
- Xue, Z., Hutchinson, J.W., 2004. A comparative study of blast-resistant metal sandwich plates. *International Journal of Impact Engineering* 30 (10), 1283–1305.